



Hollow spherical RuO₂@TiO₂@Pt bifunctional photocatalyst for coupled H₂ production and pollutant degradation

Bing Cao, Guisheng Li*, Hexing Li*

Chinese Education Key Lab of Resource Chemistry, Shanghai University of Electric Power, Shanghai 200090, China

ARTICLE INFO

Article history:

Received 3 March 2016

Received in revised form 15 April 2016

Accepted 16 April 2016

Available online 19 April 2016

Keywords:

RuO₂@TiO₂@Pt hollow spheres

Controlled assembly of RuO₂ and Pt

Coupled photocatalytic H₂ production and organics degradation

Synergetic effect

ABSTRACT

A novel bifunctional RuO₂@TiO₂@Pt photocatalyst was designed by control-assembling TiO₂ hollow spheres with RuO₂ and Pt deposited onto outer and inner shell surfaces, respectively. This RuO₂@TiO₂@Pt was used in coupled photocatalytic H₂ production and organic pollutant degradation, which showed the synergetic effect between photocatalytic oxidation and reduction. Meanwhile, the RuO₂ facilitated the transfer and collection of photo-induced holes generated from TiO₂, followed by oxidizing organic pollutants for degradation. Similarly, the Pt promoted the transfer and enrichment of photoelectrons, which favored the proton reduction to H₂ as a cocatalyst. Thus, the RuO₂@TiO₂@Pt exhibited very high activity owing to the enhanced light harvesting through multiple reflections in the TiO₂ hollow chamber, the rapid separation corresponding to the low recombination of photoelectron-hole and the cooperative promoting effect from RuO₂ and Pt cocatalysts in photocatalytic oxidation and reduction.

© 2016 Elsevier B.V. All rights reserved.

1. Introduction

With the increasing worry about energy crisis and environmental pollution [1,2], photocatalysis has attracted great attention owing to its potential in producing H₂, removing organic or metallic pollutants, and converting CO₂ [3–8]. The TiO₂ photocatalyst has been most frequently employed owing to its easy availability, high activity, strong stability, and non-toxicity, etc [9–12]. The key problems related to the photocatalytic efficiency are the light harvesting ability [13], excitation by sunlight [14], and the photoelectron-hole recombination [15], which could be improved by tailoring TiO₂ morphology [16–18], doping TiO₂ [19,20], and engineering surface chemistry [21]. Photocatalytic H₂ production from water splitting reactions has confirmed as the proton reduction by photoelectrons [22]. Methanol is usually used as the sacrificial agent to consume holes [23,24], which seems unreasonable since methanol is also an important fuel or chemical agent. Obviously, the coupled photocatalytic H₂ production and organic pollutant degradation was an ideal way for synchronously consuming photoelectrons [25]. Both the experimental results and theoretical predictions demonstrate that the Pt cocatalyst deposited on TiO₂ could enrich photoelectrons and also promote H⁺ reduction into H₂ [26,27]. Meanwhile, the RuO₂ cocatalyst deposited onto TiO₂ could collect photo-induced holes

and promote organic pollutant oxidation [28,29]. However, the random deposition of Pt and RuO₂ onto TiO₂ usually display mutual interference, leading to low photocatalytic efficiency.

Previously, we reported that the TiO₂ hollow spheres exhibited high activity in photocatalytic degradation of organic pollutants owing to the large surface area and the unique chamber for enhancing light absorbance through multiple reflections [30]. Herein, we reported for the first time the TiO₂ hollow spheres with RuO₂ and Pt nanoparticles deposited onto inner and outer surfaces, respectively. Such a RuO₂@TiO₂@Pt exhibited high efficiencies in coupled photocatalytic H₂ production and organic pollutant degradation owing to the synergetic effects from RuO₂ and Pt cocatalysts.

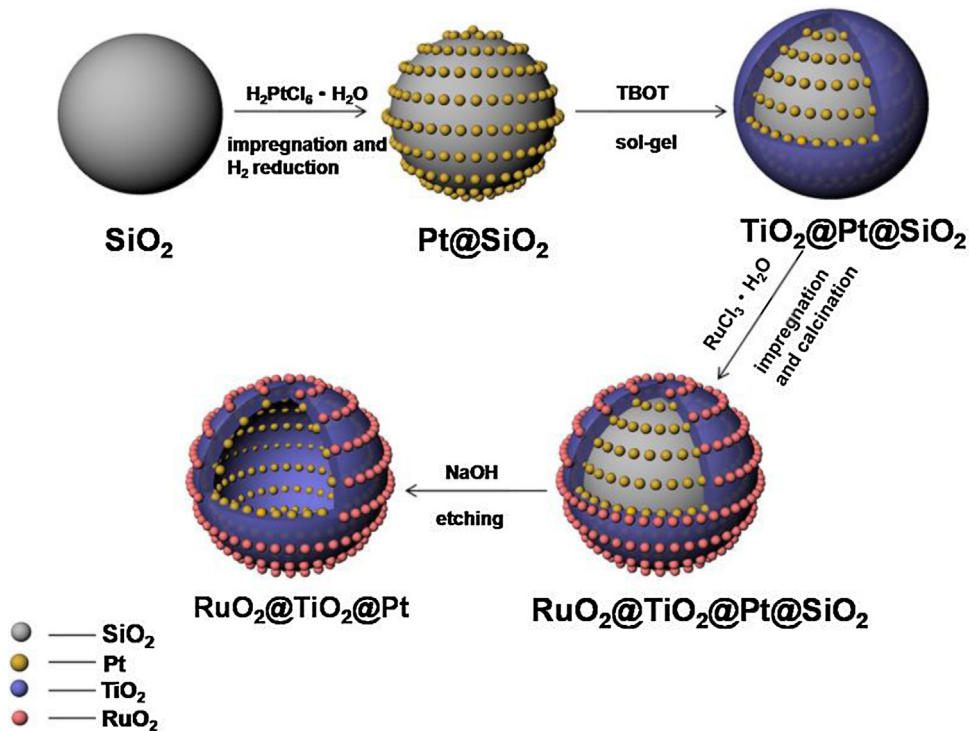
2. Experimental section

2.1. Photocatalyst preparation

Scheme 1 simply illustrated the synthesis of RuO₂@TiO₂@Pt. Firstly, uniform SiO₂ microspheres were prepared by using the classic Stober method reported elsewhere [31]. Then, Pt nanoparticles were deposited onto SiO₂ microspheres by impregnation with H₄PtCl₆ aqueous solution, followed by H₂ reduction at 300 °C for 3 h. The as-received Pt@SiO₂ was dispersed in a solution comprised of 0.10 g hydroxypropyl cellulose, 20 mL ethanol, and 0.10 mL water. After being stirred for 40 min, 5.0 mL ethanol containing 1.0 mL titanium *tert*-butoxide was injected at a rate of 0.50 mL/min, followed by refluxing at 85 °C for 2 h under vigorous stirring. The

* Corresponding authors.

E-mail address: hexing-li@shnu.edu.cn (H. Li).



solid was then isolated using centrifugation, washed thoroughly with ethanol, vacuum dried at 80 °C for 2 h, and calcined at 500 °C for 2 h. Subsequently, the as-prepared TiO₂@Pt@SiO₂ was impregnated in RuCl₃ aqueous solution at 50 °C under stirring, followed by drying at 200 °C for 12 h and calcination at 300 °C for another 4 h, leading to the RuO₂@TiO₂@Pt@SiO₂. Finally, the SiO₂ was etched away completely in 20 mL 0.50 M NaOH aqueous solution for 12 h to get RuO₂@TiO₂@Pt hollow spheres with the RuO₂ and Pt nanoparticles deposited onto the outer and inner surfaces of the TiO₂ shell, respectively. The RuO₂ and Pt loadings could be easily adjusted by changing the H₄PtCl₆ and RuCl₃ concentrations.

For comparison, Pt@TiO₂@RuO₂ with Pt and RuO₂ nanoparticles separately deposited onto the outer and inner surface of the TiO₂ shell was also synthesized in the similar way by depositing RuO₂ firstly onto SiO₂ microspheres. Meanwhile, TiO₂@Pt and RuO₂@TiO₂ with only Pt and RuO₂ nanoparticles deposited onto either inner or outer shell surface of TiO₂ hollow microspheres were also synthesized in the similar method by using only H₄PtCl₆ or RuCl₃. Besides, pure TiO₂ hollow spheres were synthesized in the same way without adding metallic sources.

2.2. Characterization

The crystal structure and morphology were determined using X-ray diffraction (XRD, D/MAX-2000 with Cu K α radiation), field emission scanning electron microscopy (FESEM, HITACHI S4800), and transmission electron microscopy (TEM, JEOL JEM-2100). Optical properties were measured by UV-vis diffuse reflectance spectroscopy (DRS, MC-2530) and photoluminescence spectroscopy (PLS, Varian Cary-Eclipse 500) excited by the light with wavelength of by exciting 390 nm. The N₂ adsorption-desorption isotherms were collected on a TriStar® II 3020 instrument at -196 °C, from which the surface area (SBET) was calculated using the BET method. The surface electronic states were analyzed by X-ray photoelectron spectroscopy (XPS, PerkinElmer PHI 5000). All the binding energy values were calibrated by using C1s = 284.6 eV as the reference.

Photoelectrochemical measurement was carried out in a conventional three-electrode, homemade single-compartment quartz cell on an electrochemical station (CHI 660D) using a 3W LED lamp (λ = 365 nm). The testing of photocurrent used the light on-off process with a pulse of 10 s by potentiostatic technique. Electrochemical impedance spectroscopy (EIS) was performed under UV light (λ = 365 nm) irradiation in a 0.50 mol/L Na₂SO₄ solution at open circuit voltage over a frequency range from 105 to 10–1 Hz with an AC voltage at 5 mV. The transient photocurrent was measured using a 20 s on-off cycle at a bias voltage of 0.5 V.

2.3. Activity test

Synergistic photocatalytic H₂ production from water splitting and degradation of various organic pollutants were carried out at 30 °C in a self-designed glass reactor containing 50 mg catalyst, 80 mL aqueous solution with desired amount of one organic pollutant (See Fig. S1). After being stirred at room temperature for 1 h to reach adsorption equilibrium, the photocatalysis was initiated by irradiating the reaction mixture with 4 LED lamps (characteristic wavelength (λ) = 365 nm) located at 1.0 cm away from the solution surface. The amount of hydrogen evolved was determined by a gas chromatograph (GC-9800, N₂ carrier gas) equipped with a thermal conductivity detector (TCD5-A). Meanwhile, the degradation yield was calculated based on the unreacted organic pollutants determined by UV spectrophotometer (UV-7504/PC) at the characteristic wavelength corresponding to each organic compound

3. Results and discussion

3.1. Structural characteristics

The XPS spectra (Fig. S2) revealed the presence of anatase TiO₂ in the RuO₂@TiO₂@Pt, corresponding to the binding energies of Ti around 458.2 and 464.2 eV in Ti2p_{3/2} and Ti2p_{1/2} levels, while, the binding energy of O was found at 529.6 eV in O1S level [32]. Before H₂ reduction, the Pt species were present in Pt⁴⁺ oxidation

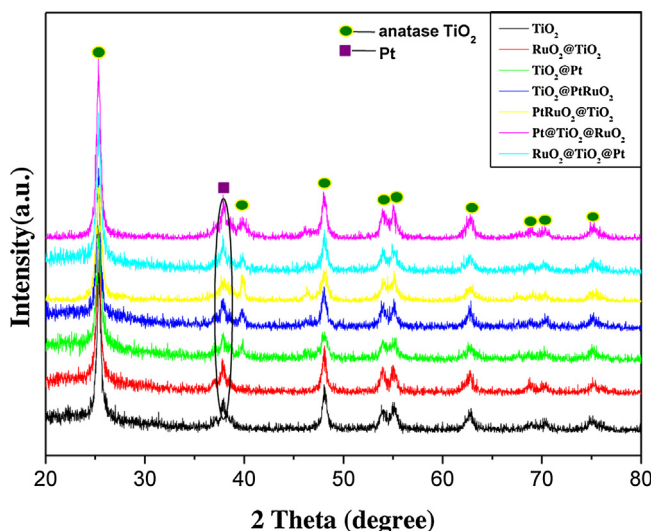


Fig. 1. XRD patterns of different photocatalysts with Pt and RuO₂ loadings of 1 wt% and 0.5 wt%, respectively.

state with binding energy around 381.1 eV in Pt4f level [33]. After H₂ reduction at 300 °C for 3 h, the original peak characteristic of Pt⁴⁺ totally disappeared and a new peak around binding energy of 70.6 eV appeared, indicating the complete reduction of Pt⁴⁺ into metallic Pt. Before calcinations, the Ru species were present in Ru³⁺ oxidation state with the binding energy around 282.0 eV in Ru3d level [34]. After calcination at 300 °C for 4 h, the original peak totally disappeared, corresponding to the appearance of a new peak with the binding energy around 279.4 eV, which could confirm the transformation of Ru³⁺ into RuO₂. The XRD patterns in Fig. 1 further confirmed that all the as-prepared samples after calcinations displayed TiO₂ anatase phase, corresponding to the principal peak around 20 of 25.81 (JCPDS No: 21-1272). Metallic Pt nanoparticles were found at 20 around 39.76 (JCPDS No: 04-0802). No significant peaks indicative of RuO₂ were observed, which could be attributed to the very low content and high dispersion.

Fig. 2 shows the FESEM and TEM images of the precursors obtained at different steps. The as-synthesized SiO₂ template was present in uniform microspheres with diameter around 300 nm. The Pt nanoparticles were highly dispersed onto the SiO₂ outer surface in the Pt@SiO₂. The TiO₂ film was uniformly coated onto the SiO₂ microspheres in the TiO₂@Pt@SiO₂. Meanwhile, the RuO₂ nanoparticles were also well dispersed onto the TiO₂ film in the RuO₂@TiO₂@Pt@SiO₂. As shown in Fig. 3, the TEM image demonstrated that the RuO₂@TiO₂@Pt obtained by etching the RuO₂@TiO₂@Pt@SiO₂ in NaOH solution for 2 h exhibited hollow microspheres owing to the complete removal of the SiO₂ core microspheres. The average shell thickness was determined as 5–7 nm. The chemical mapping images showed the circle-dispersion of RuO₂ and Pt nanoparticles. The diameter of the RuO₂ circle was slightly bigger than that of the Pt circle. Although it was not clear enough, we still concluded that the RuO₂ and Pt nanoparticles mainly dispersed respectively onto the outer and inner shell-surfaces of TiO₂ hollow spheres, respectively. On one hand, the Pt was firstly deposited on the SiO₂ core followed by coating with TiO₂ shell. So Pt nanoparticles could not appear on the outer surface of the TiO₂ shell. On the other hand, the RuO₂ were deposited directly onto the TiO₂ shell. Thus, most RuO₂ particles should locate on the outer surface of the TiO₂ shell.

The pure TiO₂ and all the Pt- and/or RuO₂-doped TiO₂ displayed type IV N₂ adsorption-desorption isotherms with a H1 type hysteresis loop, corresponding to the mesoporous structure (see Fig. S3) [35]. The similar N₂ adsorption-desorption isotherms indicated

Table 1
Structural parameters of the as-prepared photocatalysts.

Sample	S _{BET} (m ² /g)	V _P (cm ³ /g)	D _P (nm)
TiO ₂	57.7	0.159	10.2
TiO ₂ @Pt	74.8	0.417	18.9
RuO ₂ @TiO ₂	64.5	0.174	9.78
TiO ₂ @Pt/RuO ₂	75.0	0.358	19.1
Pt/RuO ₂ @TiO ₂	62.8	0.162	10.5
RuO ₂ @TiO ₂ @Pt	74.6	0.209	10.2

that the principal structural parameters were mainly contributed from TiO₂ rather than from either RuO₂ or Pt nanoparticles. The pore size distribution curve revealed that the RuO₂@TiO₂@Pt contained two kinds of pores. One was the small pore with the narrow diameter range centered at 2.0 nm, which could be attributed to the TiO₂ network. The other was the large pore with the broad diameter ranging from 5 to 30 nm due to the package of TiO₂ nanoparticles. Table 1 summarized the specific surface area (SBET), pore volume (VP) and pore size (DP) calculated based on the N₂ adsorption-desorption isotherms. The pure TiO₂ obtained by etching TiO₂@SiO₂ to remove SiO₂ exhibited lower SBET than TiO₂@Pt obtained by etching TiO₂@Pt@SiO₂ to remove SiO₂, which could be attributed to the enlarged diameter of TiO₂ shell. This could also account of the larger SBET of TiO₂@RuO₂/Pt than that of TiO₂@Pt since the diameter of TiO₂ shell was further enlarged. On contrary, the RuO₂@TiO₂ and Pt/RuO₂@TiO₂ exhibited similar SBET to the pure TiO₂ since both RuO₂ and Pt/RuO₂ were coated onto the outer surface of TiO₂ shell without change of the TiO₂ shell diameter. The RuO₂@TiO₂@Pt also displayed large SBET similar to TiO₂@RuO₂/Pt and TiO₂@Pt since the inside Pt-doping enlarged the TiO₂ shell diameter, though the RuO₂ was doped onto the outer surface.

3.2. Photoelectric characteristics

Fig. 4a shows the photoelectrochemical responses of the as-prepared samples under UV light ($\lambda = 365$ nm) irradiation. The photocurrent value alternatively increased to maximum and decreased to zero corresponding to the light turn-on and turn-off, which could be attributed to the instinct properties of all the semiconductors [36–38]. The photocurrent intensity increased from TiO₂, Pt/RuO₂@TiO₂, RuO₂@TiO₂, TiO₂@Pt/RuO₂, TiO₂@Pt, to RuO₂@TiO₂@Pt. This could be mainly ascribed to the number of photoelectrons generated by exciting the photocatalyst and the photoelectron-hole recombination rate [39]. Firstly, the UV-vis absorption spectra (DRS) in Fig. 4b revealed that all the samples showed similar light absorbance in the range 200–380 nm owing to the similar morphologies and the same anatase phase of TiO₂. This means that they generated the similar number of photoelectrons under UV light irradiation. Thus, the photocurrent intensity was mainly dependent on the photoelectron-hole recombination rate. As shown in Fig. 4c, the PLS spectra demonstrated that the intensity of the peak around 450 nm and 530 nm changed in the order of TiO₂ > TiO₂@Pt/RuO₂ ≈ Pt/RuO₂@TiO₂ > RuO₂@TiO₂ > TiO₂@Pt > RuO₂@TiO₂ ≈ RuO₂@TiO₂@Pt, indicating the gradual decrease in photoelectron-hole recombination rate [40]. This could sufficiently account for the photocurrent intensity change. The RuO₂ facilitated the transfer of photo-induced holes from TiO₂ to RuO₂, while the metallic Pt promoted the transfer of photoelectrons from TiO₂ to Pt [41]. Because RuO₂ and Pt deposited on the outer and inner TiO₂ shell surfaces, the photoelectrons and holes transferred in opposite directions, which could facilitate their separation and thus, diminish their recombination. As shown in Fig. 4d, the arc radius in the EIS Nyquist plots determined under UV light irradiation changed in the order of TiO₂ > RuO₂@TiO₂ > TiO₂@Pt/RuO₂ ≈ Pt/RuO₂@TiO₂ > Pt@TiO₂@RuO₂ ≈ RuO₂@TiO₂@Pt, indicating the gradual decrease in electric resis-

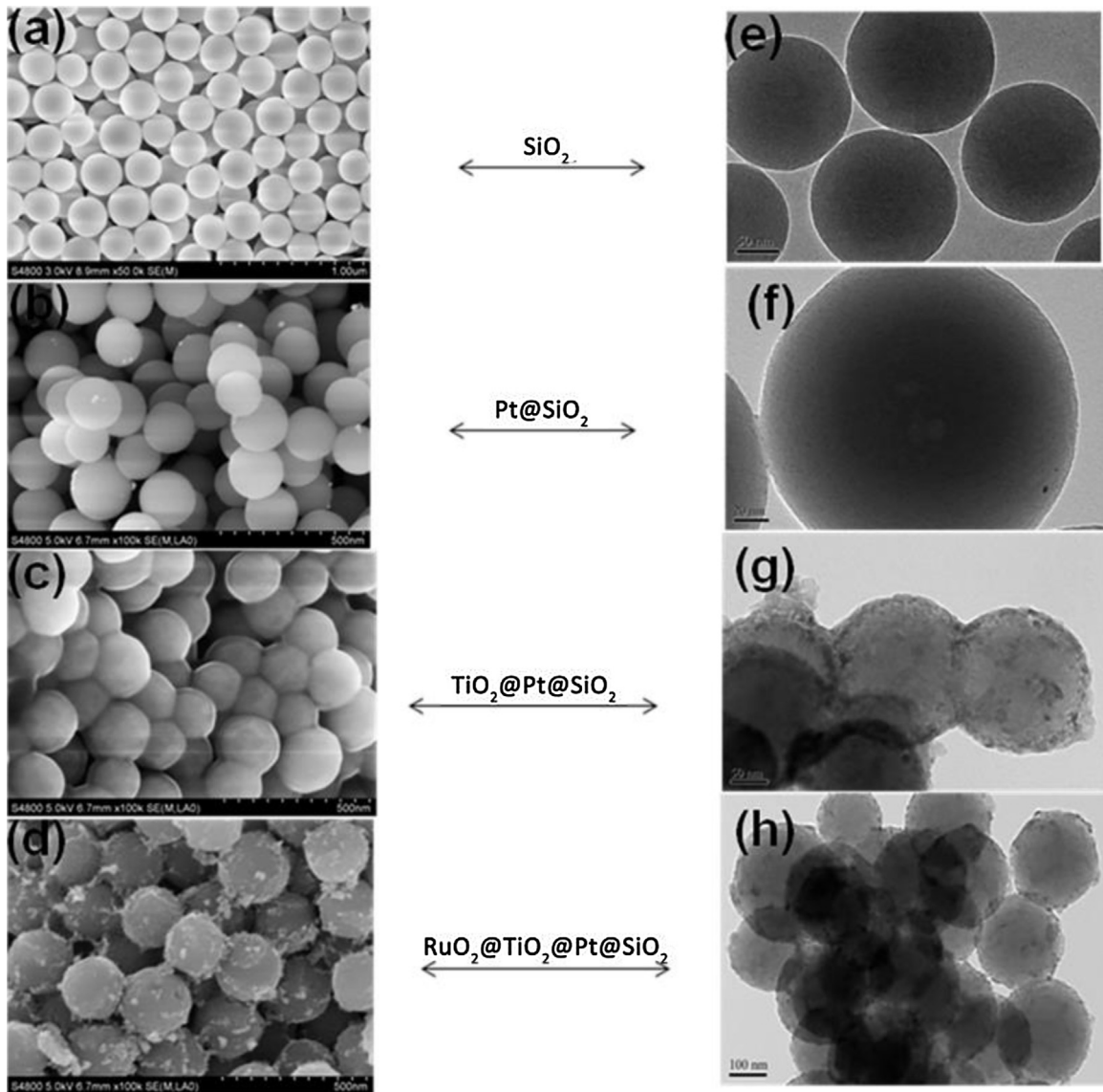


Fig. 2. FESEM (Left) and TEM (Right) images of (a, e) SiO₂, (b, f) Pt@SiO₂, (c, g) TiO₂@Pt@SiO₂, and (d, h) RuO₂@TiO₂@Pt@SiO₂. The Pt and RuO₂ loadings in all the samples are 1 wt% and 0.5 wt%, respectively.

tance [42,43]. The RuO₂@TiO₂@Pt exhibited the lowest electric resistance since the RuO₂ and Pt promoted the transfer of photoelectrons and holes toward opposite directions. This could account the higher electric resistance of either the TiO₂@Pt/RuO₂ or the Pt/RuO₂@TiO₂ since Pt and RuO₂ on the same position. The TiO₂@Pt/RuO₂ and the Pt/RuO₂@TiO₂ also exhibited higher photoelectron-hole recombination rate since the holes collected on the RuO₂ and the photoelectrons collected on Pt could easily contact and recombined, corresponding to the low photocurrent intensity. The RuO₂@TiO₂ displayed high electric resistance since RuO₂ only facilitated the transfer of holes rather than photoelectrons.

3.3. Photocatalytic performances

Scheme 2 briefly illustrated the generation, transfer, enrichment, consumption of photoelectrons and holes in RuO₂@TiO₂@Pt hollow spheres during coupled photocatalytic H₂ evolution and organic pollutant degradation. Firstly, TiO₂ semiconductor was excited by UV lights to generate photoelectrons and holes. Then, the photoelectrons and holes transferred and collected onto Pt and

RuO₂, respectively. Finally, the Pt and RuO₂ co-catalysts initiated the proton reduction to produce H₂ and the oxidation of organic pollutant to CO₂, respectively.

Fig. 5 demonstrated the optimum Pt and RuO₂ loadings of 1 wt% and 0.5 wt%, respectively. The H₂ evolution rate first increased with increasing Pt loading up to 1 wt% owing to the increase of Pt active sites. However, very high Pt loading was harmful due to the gathering of Pt nanoparticles, which disfavored the proton reduction and may also serve as the center of photoelectron-hole recombination. Similarly, the H₂ evolution rate increased with increasing RuO₂ loading up to 0.5 wt% owing to the increase of RuO₂ active sites. Further increase in RuO₂ loading resulted in abrupt decreased activity because the gathering of RuO₂ nanoparticles, which may serve as the center of photoelectron-hole recombination.

Based on the RuO₂@TiO₂@Pt photocatalyst with optimal RuO₂ and Pt loadings, the H₂ evolution rate in pure water and aqueous solution containing different alcohols as model pollutants were determined. As shown in **Fig. 6**, only trace H₂ evolution was found in pure water and the addition of alcohols in water could greatly enhance the H₂ evolution rate. The H₂ evolution rate increased gradually from tert.-butyl alcohol (t-BuOH), *n*-butanol (*n*-BuOH),

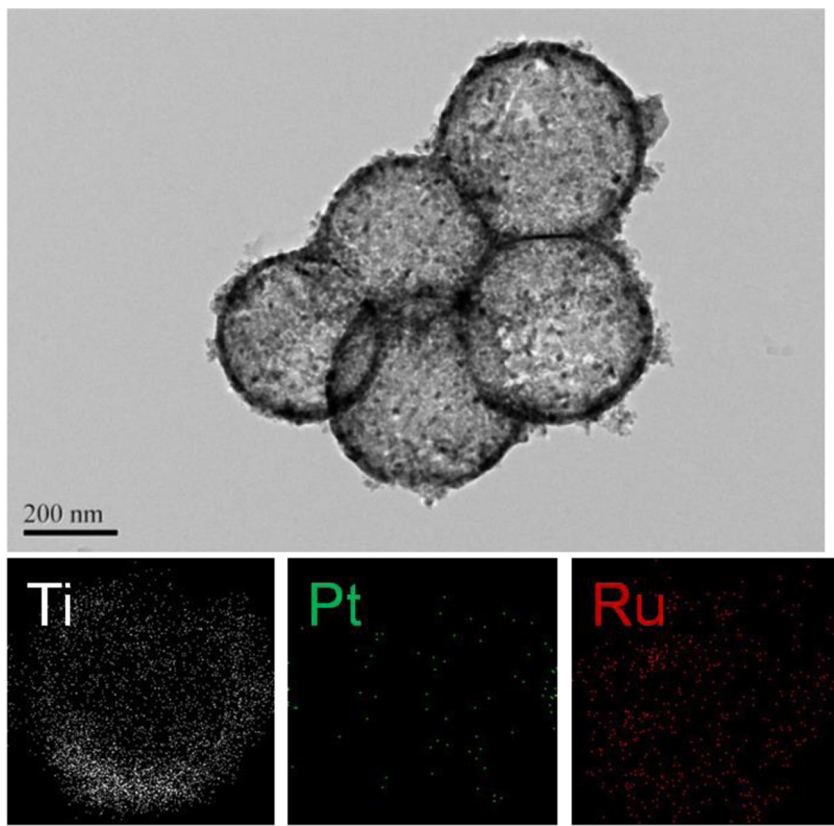


Fig. 3. TEM image and chemical mappings of $\text{RuO}_2@\text{TiO}_2@\text{Pt}$ with Pt and RuO_2 loadings of 1 wt% and 0.5 wt%.

n-propanol (*n*-PrOH), ethanol (EtOH), to methanol (MeOH) since the degradation of those alcohols became gradually easier. By using real organic pollutants like phenol, RhB (rhodamine B) and MO (methyl orange), we determined both the H_2 evolution rate and the degradation yield. It was found that, with the increasing degradation yield from RhB (98%) to MO (80%) to phenol (40%), the H_2 evolution rate also increased from 809 to 748 to 405 $\mu\text{mol}/\text{g}\cdot\text{h}$. These results clearly demonstrated the synergistic effect between photocatalytic H_2 evolution and organic pollutant degradation. To further confirm the roles played by coupled photocatalytic oxidation-reduction, we determined the H_2 evolution rates in the presence of different organic pollutants by using $\text{RuO}_2@\text{TiO}_2@\text{Pt}$ and $\text{Pt}@\text{TiO}_2@\text{RuO}_2$ photocatalysts, respectively. In $\text{RuO}_2@\text{TiO}_2@\text{Pt}$, the RuO_2 was deposited on the outer surface of TiO_2 shell while the Pt was deposited on the inner surface. On contrast, in $\text{Pt}@\text{TiO}_2@\text{RuO}_2$, the RuO_2 and the Pt was deposited on the inner and outer surfaces of TiO_2 shell, respectively. Fig. 7 shows the H_2 evolution rate ratios between $\text{RuO}_2@\text{TiO}_2@\text{Pt}$ and $\text{Pt}@\text{TiO}_2@\text{RuO}_2$ (n_1/n_0). Firstly, we found that $\text{RuO}_2@\text{TiO}_2@\text{Pt}$ exhibited higher H_2 evolution rate than the $\text{Pt}@\text{TiO}_2@\text{RuO}_2$ regardless of the organic substances used as model pollutants. Meanwhile, we also found that the n_1/n_0 decreased gradually with the increasing molecular size of the organic compounds. As mentioned above, both $\text{RuO}_2@\text{TiO}_2@\text{Pt}$ and $\text{Pt}@\text{TiO}_2@\text{RuO}_2$ displayed the similar light harvesting abilities, energy band gaps, photocurrent intensities, photoelectron-hole recombination rates and structural parameters (SBET, VP and DP). Taking into account that the RuO_2 and Pt served as active sites for photocatalytic oxidation and reduction, respectively, we concluded that the different H_2 evolution rates on those two photocatalysts were mainly ascribed to the diffusion limit of organic molecules since the diffusion limit of protons with extremely small size could be neglected. The organic pollutants in aqueous solution could directly contact the RuO_2 on the outer

surface of the TiO_2 shell in $\text{RuO}_2@\text{TiO}_2@\text{Pt}$. However, the organic pollutants should undergo a diffusion process to pass through TiO_2 shell for contacting the RuO_2 on the inner surface in $\text{Pt}@\text{TiO}_2@\text{RuO}_2$. This could account for the higher activity of $\text{RuO}_2@\text{TiO}_2@\text{Pt}$ than that of $\text{Pt}@\text{TiO}_2@\text{RuO}_2$ since no diffusion process was needed for the $\text{RuO}_2@\text{TiO}_2@\text{Pt}$. It could also account for the decreased n_1/n_0 with the increasing size of organic molecules since the diffusion limit increased. We also determined the photocatalytic activities of crushed $\text{Pt}@\text{TiO}_2@\text{RuO}_2$ and crushed $\text{RuO}_2@\text{TiO}_2@\text{Pt}$ (Fig. S4). Their similar activities further confirmed the important effect of organic pollutant diffusion on the H_2 evolution rate since the crushed photocatalysts did not show such a configurational (inside/outside) dependency and provided similar efficient access of organic pollutants to the RuO_2 site.

In comparison with the $\text{RuO}_2@\text{TiO}_2@\text{Pt}$ after being crushed by grinding, the $\text{RuO}_2@\text{TiO}_2@\text{Pt}$ in hollow spheres showed higher activity (Fig. S5), which could be attributed to the enhanced light harvesting through multiple reflections inside the chamber (see the attached diagram) [44]. In addition, we also found that the photocatalytic activity of $\text{RuO}_2@\text{TiO}_2@\text{Pt}$ first increased and then decreased with the increase of TiO_2 shell thickness (Fig. S6). The optimal TiO_2 shell thickness was determined as 5–7 nm. The $\text{RuO}_2@\text{TiO}_2@\text{Pt}$ with very thin TiO_2 shell exhibited low activity since the hollow structure was unstable and could be easily broken up. Meanwhile, RuO_2 and Pt may directly contact at very thin TiO_2 shell, which could enhance the photoelectron-hole recombination. Very thick TiO_2 shell was also harmful for the photocatalytic activity of the $\text{RuO}_2@\text{TiO}_2@\text{Pt}$ due to the enhanced diffusion limit and the decreased light absorbance of the inner-layer TiO_2 . The TEM image of the used $\text{RuO}_2@\text{TiO}_2@\text{Pt}$ photocatalyst with shell thickness of 5–7 nm (Fig. S7) demonstrated that the hollow structure was preserved.

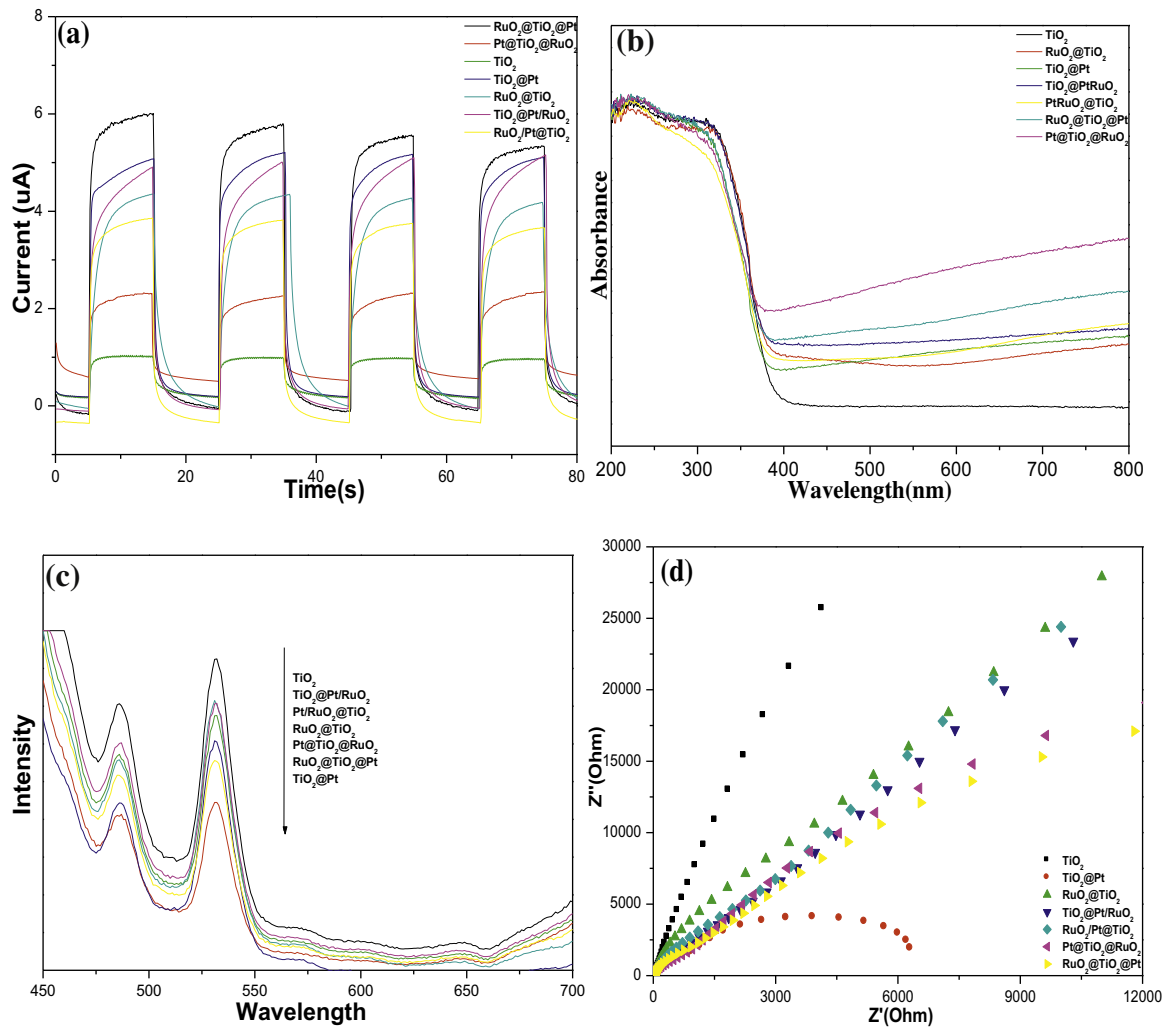


Fig. 4. Photocurrent spectra (a), UV-vis spectra (b), PL spectra (c) and electrochemical impedance spectroscopy (d) of different photocatalysts. The Pt and RuO_2 loadings in all the samples are 1 wt% and 0.5 wt%, respectively.

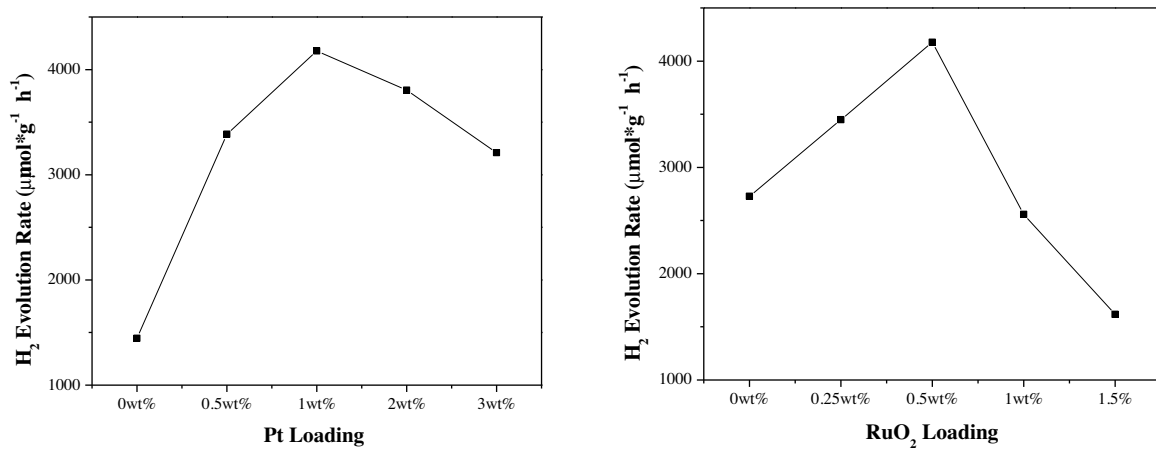
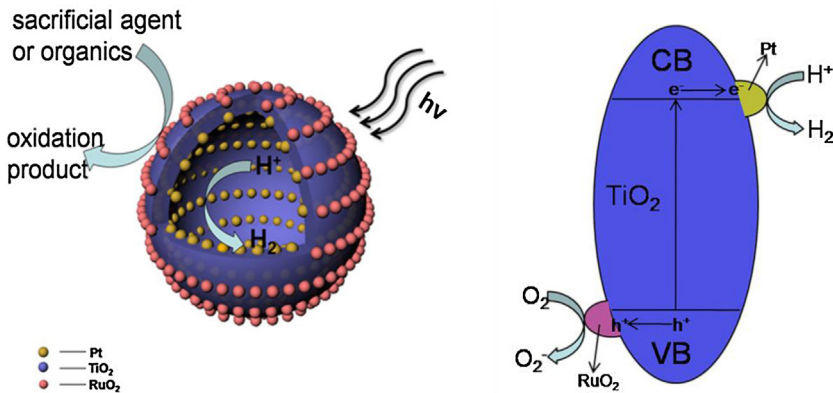


Fig. 5. Dependence of photocatalytic activity of $\text{RuO}_2@\text{TiO}_2@\text{Pt}$ on Pt or RuO_2 loading. Reaction conditions: 50 mg photocatalyst, 80 mL aqueous solution comprised of 60 mL water and 20 mL methanol, 4 LED lamps with characteristic λ of 365 nm located at 1.0 cm away from the solution, 30 °C.

Fig. 8 shows the H_2 evolution rates determined on different photocatalysts present in hollow spheres. The pure TiO_2 exhibited the lowest activity due to the absence of cocatalysts and the high photoelectron-hole recombination rate. The $\text{RuO}_2@\text{TiO}_2$ was more active than the pure TiO_2 since the RuO_2 promoted

photoelectron-hole separation and could also served as active sites for the oxidation of organic pollutants [45]. The $\text{TiO}_2@\text{Pt}$ also exhibited enhanced activity since Pt promoted photoelectron-hole separation and could serve as active sites for proton reduction. The $\text{TiO}_2@\text{Pt}$ displayed remarkably higher activity than the



Scheme 2. Illustration of the photocharge transfer and separation as well as consumption in the RuO₂@TiO₂@Pt during coupled photocatalytic H₂ production and organic pollutant degradation.

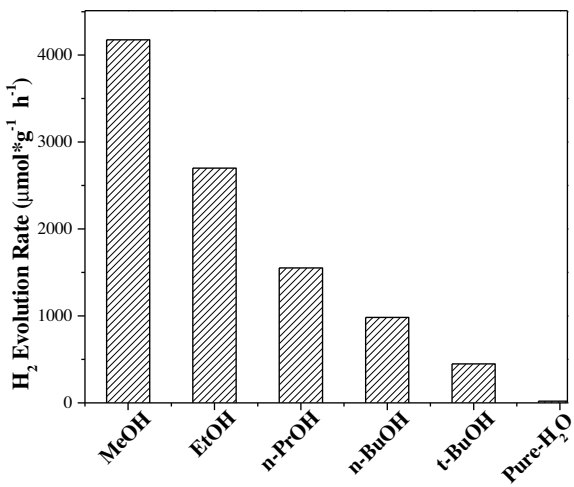


Fig. 6. H₂ evolution rate on RuO₂@TiO₂@Pt photocatalyst at Pt and RuO₂ loadings of 1 wt% and 0.5 wt% in pure water and in water containing different alcohols as model organic pollutants. Reaction conditions are given in Fig. 5.

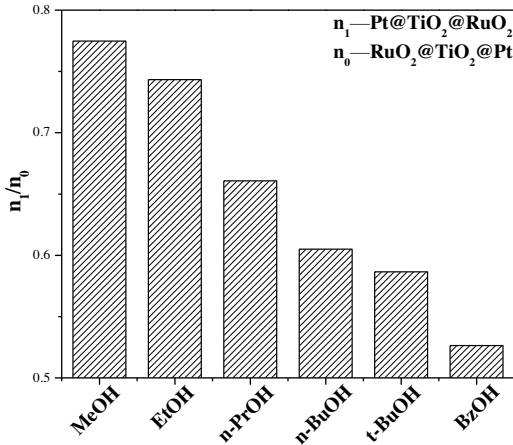


Fig. 7. Photocatalytic H₂ evolution of RuO₂@TiO₂@Pt and Pt@TiO₂@RuO₂. The Pt and RuO₂ loadings in all the samples are 1 wt% and 0.5 wt%, respectively. Reaction conditions are given in Fig. 5.

RuO₂@TiO₂ since the photoelectron transfer through Pt was more efficient than the hole transfer through RuO₂ and also the Pt was the direct cocatalyst for H₂ production. The RuO₂@TiO₂@Pt was the most active photocatalyst because of the synergetic effect of Pt and RuO₂. Interestingly, both the Pt/RuO₂@TiO₂

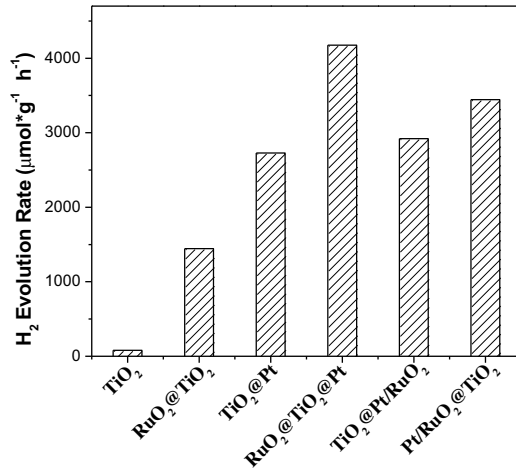


Fig. 8. H₂ evolution rates on different photocatalysts with Pt and/or RuO₂ loadings of 1 wt% and 0.5 wt%, respectively. Reaction conditions are given in Fig. 5.

and the TiO₂@Pt/RuO₂ showed slightly lower activities than the RuO₂@TiO₂@Pt since the direct contact of RuO₂ and Pt nanoparticles would reduce the photoelectron-hole separation efficiency. Although the similar structural parameters and photoelectrical properties, Pt/RuO₂@TiO₂ displayed slightly higher H₂ evolution rate than TiO₂@Pt/RuO₂, which further confirmed the influence from diffusion limit of organic pollutants.

4. Conclusions

We developed a new RuO₂@TiO₂@Pt photocatalyst by controlling assembling RuO₂ and Pt nanoparticles onto the outer and inner shell surfaces of TiO₂ hollow spheres, respectively. The RuO₂ and Pt served as cocatalysts for photocatalytic oxidation and reduction, respectively. They also facilitated the transfer and enrichment of photoelectrons and holes. As a result, the RuO₂@TiO₂@Pt exhibited high activity in coupled H₂ production and organic pollutant degradation under UV light irradiation. This work supplied a powerful method to design efficient photocatalysts for coupled H₂ production and organic pollutant degradation. Meanwhile, it also supplied strong evidences for deep insight of the photocatalytic mechanism.

Acknowledgements

This work was supported by the National Natural Science Foundation of China (21237003), Shanghai Government (14JC1402500, 15520711300), PCSIRT (IRT1269), and Shanghai Key Laboratory.

Appendix A. Supplementary data

Supplementary data associated with this article can be found, in the online version, at <http://dx.doi.org/10.1016/j.apcatb.2016.04.033>.

References

- [1] J.G. Yu, J.R. Ran, *Energy Environ. Sci.* 4 (2011) 1364–1371.
- [2] S.P. Xu, D.D. Sun, *Int. J. Hydrogen Energy* 34 (2009) 6096–6104.
- [3] A. Fujishima, K. Honda, *Nature* 238 (1972) 37–38.
- [4] J. Zhang, Q. Xu, Z. Feng, M. Li, C. Li, *Angew. Chem. Int. Ed.* 47 (2008) 1766–1769.
- [5] Q. Lin, Y. Huang, Y. Wang, L. Li, X.Y. Liu, F. Lv, A. Wang, W.C. Li, T. Zhang, *J. Mater. Chem. A* 2 (2014) 5178–5181.
- [6] J.B. Joo, Q. Zhang, I. Lee, M. Dahl, F. Zaera, Y. Yin, *Adv. Funct. Mater.* 22 (2012) 166–174.
- [7] D. Wang, T. Hisatomi, T. Takata, C. Pan, M. Katayama, J. Kubota, K. Domen, *Angew. Chem. Int. Ed.* 125 (2013) 1–5.
- [8] Z.F. Bian, J. Zhu, F. Cao, F. Lu, H. Li, *Chem. Commun.* (2009) 3789–3791.
- [9] M.A. Henderson, *Surf. Sci. Rep.* 66 (2011) 185–297.
- [10] X.Q. Gong, A. Selloni, O. Dulub, P. Jacobson, U. Diebold, *J. Am. Chem. Soc.* 130 (2008) 370–381.
- [11] C.L. Pang, R. Lindsay, G. Thornton, *Chem. Soc. Rev.* 37 (2008) 2328–2353.
- [12] U. Diebold, *Surf. Sci. Rep.* 48 (2003) 53–229.
- [13] C. Chen, W. Ma, J. Zhao, *Chem. Soc. Rev.* 39 (2010) 4206–4219.
- [14] L. Gomathi Devi, R. Kavitha, *RSC Adv.* 4 (2014) 28265–28299.
- [15] R. Li, H. Han, F. Zhang, D. Wang, C. Li, *Energy Environ. Sci.* 7 (2014) 1369–1376.
- [16] J. Sorapong, S. Yoshikazu, Y.K. Susumu, Y.K. Japa, *J. App. Phys.* 47 (2008) 751–756.
- [17] H.Q. Wang, Z.B. Wu, Y. Liu, *J. Phys. Chem. C* 113 (2009) 13317–13324.
- [18] S. Chuangchote, J. Jitputti, T. Sagawa, S. Yoshikawa, *ACS Appl. Mater. Interfaces* 1 (2009) 1140–1143.
- [19] S. Sakthivel, S.M. Venkatakrishnan, M. Palanichamy, B. Arabindoo, D.W. Bahnermann, V. Murugesan, *Water Res.* 38 (2004) 3001–3008.
- [20] H. Xue, Z.H. Li, L.J. Zhu, *Chin. J. Struct. Chem.* 29 (2010) 1828–1833.
- [21] T. Bak, W. Li, J. Nowotny, A.J. Atanacio, J. Davis, *J. Phys. Chem. A* 119 (2015) 9465–9473.
- [22] T. Tachikawa, S. Yamashita, T. Majima, *J. Am. Chem. Soc.* 133 (2011) 7197–7204.
- [23] W. Wang, S. Liu, L. Nie, B. Cheng, J. Yu, *Phys. Chem. Chem. Phys.* 15 (2013) 12033–12039.
- [24] L. Kuang, W. Zhang, *RSC Adv.* 6 (2016) 2479–2488.
- [25] X. Lang, W.R. Leow, J. Zhao, X. Chen, *Chem. Sci.* 6 (2015) 1075–1082.
- [26] G. Tian, H. Fu, L. Jing, B. Xin, K. Pan, *J. Phys. Chem. C* 112 (2008) 3083–3089.
- [27] J.B. Joo, Q. Zhang, M. Dahl, I. Lee, J. Goebl, F. Zaera, Y. Yin, *Energy Environ. Sci.* 5 (2012) 6321–6327.
- [28] Q. Lin, Y. Huang, Y. Wang, L. Li, X.Y. Liu, F. Lv, A. Wang, W.C. Li, T. Zhang, *J. Mater. Chem. A* 2 (2014) 5178–5181.
- [29] E.V. Kondratenko, A.P. Amrute, M.M. Pohl, N. Steinfeldt, C. Mondelli, J. Perez-Ramirez, *Catal. Sci. Technol.* 3 (2013) 2555–2558.
- [30] H. Nakamura, M. Ishii, A. Tsukigase, M. Harada, H. Nakano, *Langmuir* 21 (2005) 8918.
- [31] W. Stöber, A. Fink, E. Bohn, *J. Colloid Interface Sci.* 26 (1968) 62–69.
- [32] Z.F. Jiang, J. Zhu, D. Liu, W. Wei, J. Xie, M. Chen, *CrystEngComm* 16 (2014) 2384–2394.
- [33] Z. Yang, N. Zhang, Y. Cao, M. Gong, M. Zhao, Y. Chen, *Catal. Sci. Technol.* 4 (2014) 3032–3043.
- [34] Z. Guo, C. Li, J. Liu, X. Su, Y. Wang, Y. Xia, *J. Mater. Chem. A* 3 (2015) 21123–21132.
- [35] B. Wang, X.Y. Lu, L.K. Yu, J. Xuan, M.K.H. Leung, H. Guo, *CrystEngComm* 16 (2014) 10046–10055.
- [36] Z. Lian, P. Xu, W. Wang, D. Zhang, S. Xiao, X. Li, G. Li, *ACS Appl. Mater. Interfaces* 7 (2015) 4533–4540.
- [37] G. Li, Z. Lian, X. Li, Y. Xu, W. Wang, D. Zhang, F. Tian, H. Li, *J. Mater. Chem. A* 3 (2015) 3748–3756.
- [38] G. Li, B. Jiang, S. Xiao, Z. Lian, D. Zhang, J.C. Yu, H. Li, *Environ. Sci. Processes Impacts* 16 (2014) 1975–1980.
- [39] G. Li, L. Wu, F. Li, P. Xu, D. Zhang, H. Li, *Nanoscale* 5 (2013) 2118–2125.
- [40] H. Xue, Z.H. Li, L.J. Zhu, Chin. J. Struct. Chem. 29 (12) (2010) 1828–1833.
- [41] W. Wei, Y. Dai, B. Huang, X. Li, F. Nägele, H. Over, M.H. Whangbo, T. Jacob, *J. Phys. Chem. C* 119 (2015) 12394–12399.
- [42] W.H. Leng, Z. Zhang, J.Q. Zhang, C.N. Cao, *J. Phys. Chem. B* 109 (2005) 15008–15023.
- [43] H. Zhang, R.L. Zong, J.C. Zhao, Y.F. Zhu, *Environ. Sci. Technol.* 42 (2008) 3803–3807.
- [44] J. Wang, X. Li, X. Li, J. Zhu, H. Li, *Nanoscale* 5 (2013) 1876–1881.
- [45] F. Lin, D. Wang, Z. Jiang, Y. Ma, J. Li, R. Li, C. Li, *Energy Environ. Sci.* 5 (2012) 6400–6406.